JCTC Journal of Chemical Theory and Computation

pubs.acs.org/JCTC Article

pyEF: A Python Framework for QM and QM/MM Atom-Wise Electric Field Analysis

Melissa T. Manetsch, David W. Kastner, Yuriy Román-Leshkov, and Heather J. Kulik*

Cite This: https://doi.org/10.1021/acs.jctc.6c00065 Read Online

ABSTRACT: We introduce pyEF, a software package for computing molecular electric fields, electrostatic interaction energies, and electrostatic potentials from quantum mechanical (QM) atom-centered multipole expansions with atom-wise decomposable contributions. We demonstrate the computational efficiency and accuracy of this QM-derived electric field evaluation tool through several tests. To assess the influence of the underlying QM method and charge partitioning scheme on these electrostatic quantities, we analyze over 250 configurations of an acetone solute molecule in five solvents of variable polarity. We find that electric field calculations are highly sensitive to the choice of charge partitioning method. Even among real-space charge schemes, acetone Stark tuning rates differ by up to a factor of 2. Benchmarking computed solvent dipole moments against experimental bulk values, we conclude that the CM5, ADCH, and Hirshfeld-I charge schemes most reliably capture solvent electrostatics and therefore provide a more faithful foundation for computing electric fields. When constructed from these real-space charges, electric fields are nearly insensitive to basis set size and monotonically increase in magnitude with higher Fock exchange. We also demonstrate efficient convergence of QM electrostatics when more distant molecules are represented solely by MM point charges, reducing computational overhead. Leveraging these findings, we demonstrate the use of pyEF to deduce environmental effects on a transition metal complex from a $Ga_4L_6^{12-}$ nanocage and quantify the dominant role of organic linkers in orchestrating electrostatic preorganization.

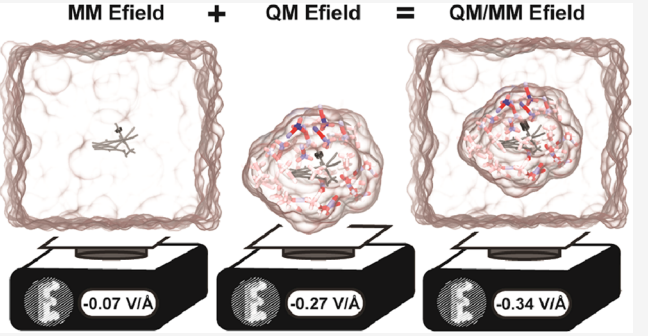

1. INTRODUCTION

Electrostatic preorganization is increasingly recognized as a central driving force in catalytic reactions. Warshel first proposed that strong electric fields exist within enzyme active sites and play a crucial role in enzymatic rate enhancement.[1,2] Three decades later, Stark spectroscopy revealed a linear correlation between the electric field experienced by a probe molecule within the ketosteroid isomerase active site and the catalytic rate.[3] Since then, strong electric fields have been implicated in catalysis across a wide range of chemical systems including enzymes,[4] transition metal complexes,[5] solid−liquid interfaces,[6] and liquid−liquid interfaces.[7,8] Collectively, these studies indicate that electric field magnitude and orientation constitute powerful knobs to control kinetics[9−13] and may serve as unifying descriptors of catalysis across chemical domains.[9,14] This vision has already been realized by imposing external potential gradients via potentiostats or scanning tunneling microscope tips. In these systems, electric fields along potential gradients have accelerated Diels−Alder reactions,[15−17] epoxide rearrangements,[18] alkoxyamine cleavages,[19] Menshutkin reactions,[20,21] and Bronsted-acid catalyzed reactions,[22] among others.[23] However, in molecular systems, *in situ* electric fields are difficult to tune and are typically quantified indirectly by mapping a vibrational frequency shift to an electric field via a Stark tuning rate.[24,25] Most Stark tuning rates are derived via electrostatic models[26] or correlations between experimental vibrational frequency measurements and computationally modeled electric fields[27] since experimental frozen solvent setups are plagued by local field effects[28] and thus require correction factors.[29] Existing quantum chemical simulations have yielded valuable insights into the limits of the linear Stark tuning regime.[30,31] Polarizable force fields have been shown to reproduce both electric fields evaluated at DFT level[32] and experimental observables,[33,34] enabling expansion of these studies to larger systems. However, comparatively little is known about the sensitivity of electric field calculations to the parameters of quantum mechanical (QM) and quantum mechanical molecular mechanics (QM/MM) simulations.

Because electrostatic interactions decay slowly with the inverse of distance[35,36] and fluctuate dynamically,[34,35,37] electric fields are often computed from MM force fields to

Received: January 13, 2026
Revised: March 5, 2026
Accepted: March 9, 2026

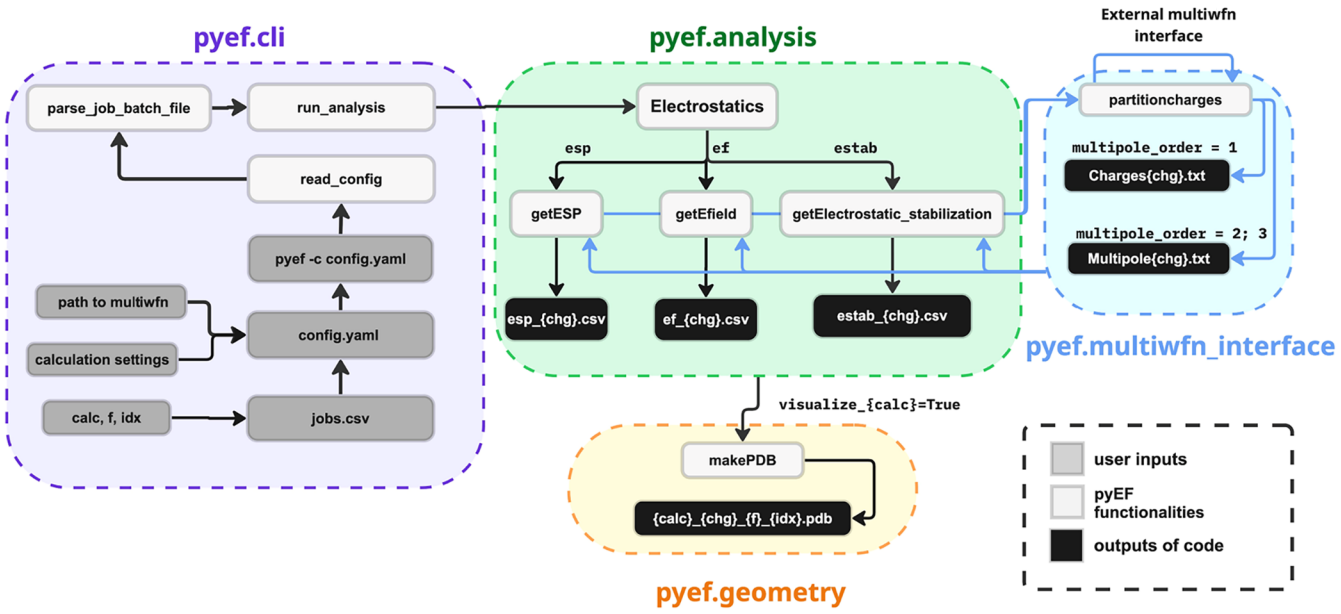

Figure 1. Overview of pyEF package structure highlighting the crucial user-facing functions. User inputs are highlighted in dark gray, code outputs are highlighted in black, and pyEF functions are highlighted in light gray. The variable calc refers to the type of calculation, including electric fields (ef), electrostatic potentials (esp), and total electrostatic stabilization energies (estab). The variable chg refers to the type of QM charge partitioning scheme, f is the path to the molden and xyz files for each job, and idx refers to the atom, bond, or substrate indices at which electrostatic properties are computed.

minimize computational expense.[38−42] In highly polar environments, intramolecular polarization must be accounted for in order to even qualitatively reproduce experimental measures of local electrostatics.[43] While in many cases electric fields computed with polarizable force fields show high parity with QM-level models,[32−34,44] these models generally cannot resolve intermolecular charge transfer or changes in bond topology. Therefore, QM-level treatement is required to understand the role of electric fields in catalytic cycles,[45−47] on proton transfer,[48] and resolve the complexities in vibrational spectra that often arise from charge transfer or charge penetration effects.[49−51]

While machine-learning interatomic potentials could eventually reduce the cost of ab initio molecular dynamics for large systems,[52] models that capture atomic multipole moments and long-range electrostatics with high fidelity are still in the earliest stages of development. Therefore, QM/MM approaches currently offer a robust compromise between accuracy and cost. Given the slow convergence of QM/MM with QM size,[53−57] it is crucial to select the smallest possible QM region and the cheapest faithful QM method to interrogate electric fields in large catalytic systems. While previous studies have demonstrated that fixed-charge molecular dynamics, polarizable force fields,[33] and QM/MM[58] models result in different computed electric field values, it remains unclear how sensitive these values are to the QM/MM region and QM method.[59,60]

To advance an understanding of electric fields in catalytic systems, electric field calculation methods must interface with numerous QM and QM/MM codes, provide atom-wise decomposability, and employ charge and multipole partitioning schemes. While several QM-level approaches are available through QChem,[61−63] these methods are cost prohibitive for long-range interactions. Classical electric field calculations provide a more affordable description of long-range electrostatics derived from atomic charges in Tupã,[40] PyCPET,[41] and TinkerModeller packages,[42] or from polarizable multipole moments in the ELECTRIC package.[39] The TITAN package[64] integrates MM point charges with QM-level NBO partial charges[65−67] but exclusively relies on the commercial Gaussian software for QM-level analysis and lacks flexibility in terms of partial charge schemes. As a result, there remains a need for an electric field calculation tool that is widely compatible with multiple QM codes and combines real-space electron density partitioning with fixed-charge representations.

To fill these gaps, we introduce pyEF, an open-source software package designed to compute electric fields and electrostatic stabilization energies in QM and mixed QM/MM systems with full atom-wise decomposability. The pyEF code supports tunable charge and multipole representations by requiring only a molecular orbital Molden file, which can be generated by most QM and QM/MM codes. To assess the most affordable computational approach to characterize electrostatic environments, we quantify how the underlying QM method and partial charge scheme impact computed electric fields. We evaluate which protocols are most robust for reproducing trends in experimental physical observables with well-established electrostatic origins, such as solvent dipole moments and vibrational Stark tuning rates. This QM and QM/MM approach allows us to affordably model large catalytic active sites. We display the utility of this approach by decomposing electrostatic contributions from cage linker functionalities and metal groups exerted by a highly polarized $Ga_4L_6^{12-}$ cage on a bound reaction intermediate.[68−70] By quantifying the effect of each building block in this modular system, we identify target synthetic modifications for optimizing electrostatic preorganization.

https://doi.org/10.1021/acs.jctc.6c00065
J. Chem. Theory Comput. XXXX, XXX, XXX−XXX

2. SOFTWARE OVERVIEW

2.1. The pyEF Package

The pyEF package is constructed with an object-oriented framework written in Python 3.8+. This package consists of a user-facing command line interface (`pyef.cli`), a core electrostatic calculation class (`pyef.analysis`), an automated interface with Multiwfn[71,72] (`pyef.multiwfn_interface`), and utility scripts to visualize atom-wise electrostatics (`pyef.geometry`, `pyef.utility`) (Figure 1).

Users can interact with pyEF in Python by directly creating an `Electrostatics` object or via the command line interface (CLI). In the CLI, users supply a single `config.yaml` script to initiate the full calculation pipeline. This `config.yaml` script requires a list of jobs to run (`jobs.csv`) and a path to the Multiwfn installation (Supporting Information Figure S1). Users can customize the calculation further by specifying optional variables including the multipole order, the QM charge-partitioning method and the location of MM point charges (Figure 1 and Supporting Information Figure S1). Each job requires a molecular geometry in an xyz file format and an associated Molden file, which is routinely generated by many quantum chemistry codes including TeraChem, Psi4, Orca, and QChem. The `cli.read_config` function processes the yaml configuration file and calls `cli.parse_job_batch_file` to parse the job list after which `cli.run_config` initiates electrostatic calculations for each job. All electrostatic calculations begin with an instantiation of a single `Electrostatics` object that organizes calculation settings and molden, xyz, and if applicable, point charge files required for the full batch of calculations. Each job type, i.e., `esp` for atom-based electrostatic potentials, `ef` for bond-wise electric fields, or `estab` for electrostatic stability, will call the associated `method: getESP()`, `getEfield()`, or `getElectrostatic_stabilization()`.

These electrostatic property functions have parallel structures. First, they each call the `partitioncharges` function in the `pyef.multiwfn_interface`, which either i) locates the appropriate `Charges_{chg_type}.txt` or `Multipole{chg_type}.txt` files or ii) interfaces with Multiwfn to partition the converged electron density into atomic charges or atom-centered multipoles. Partitioned charges or multipoles are saved as `Charges{chg_type}.txt` or `Multipole_{multi_type}.txt` files for subsequent calculations. Once charge or multipole information is collected, each of the electrostatic analysis functions launches either a monopole- or multipole-level evaluation of the property of interest and stores the associated data in a csv file in the working directory. If the user selects the visualization mode associated with the calculation (`visualize_{calc}=True`), a PDB file will be generated for each structure and the atom-wise contributions to the electrostatic property will be encoded in the B-factor column for visualization in VMD, PyMOL, ChimeraX, or any other code that supports B-factor coloring. Finally, the calculation results for all jobs of a given calculation type and a given charge scheme are recorded in a single csv file.

2.2. Electrostatic Calculations

When running monopole calculations, the first-order electric field, $\boldsymbol{E}^{(1)}(j)$ exerted by a set of environmental atoms $i \in N_{\text{env}}$ on atom j is calculated from partial charges q_i of environmental atoms and the displacement $\boldsymbol{r}_{ij}$ between the nuclear center of atoms i and j (eq 1 and Supporting Information Text S1).

$$\boldsymbol{E}^{(1)}(j) = \frac{-kC_e}{\epsilon_r} \sum_{i \in N_{\text{env}}} q_i \frac{\boldsymbol{r}_{ij}}{\left\|\boldsymbol{r}_{ij}\right\|^3} \tag{1}$$

Here, k refers to the Coulomb constant and C_e refers to the elementary charge (eq 1). The dielectric constant ϵ_r is set to unity but can be adjusted to account for screening by a solvent or confined environment.

Second- and third-order electric fields, $\boldsymbol{E}^{(2)}(j)$ and $\boldsymbol{E}^{(3)}(j)$ are calculated by a distributed multipole expansion built from the dipoles $\boldsymbol{\mu}^i$ and traceless, symmetric quadrupole tensors, $\boldsymbol{\Theta}^i$ of each atom i in the environment (eq 2 and Supporting Information Text S1).[73]

$$\boldsymbol{E}^{(3)}(j) = \frac{kC_e}{\epsilon_r} \sum_{i \in N_{\text{env}}} \left(-\frac{\boldsymbol{r}_{ij} q_i}{\left\|\boldsymbol{r}_{ij}\right\|^3} + \frac{3\boldsymbol{r}_{ij}(\boldsymbol{\mu}^i \cdot \boldsymbol{r}_{ij})}{\left\|\boldsymbol{r}_{ij}\right\|^5} - \frac{\boldsymbol{\mu}^i}{\left\|\boldsymbol{r}_{ij}\right\|^3} - \frac{5\boldsymbol{r}_{ij}(\boldsymbol{r}_{ij}^{\,T} \boldsymbol{\Theta}^i \boldsymbol{r}_{ij})}{\left\|\boldsymbol{r}_{ij}\right\|^7} + \frac{2\boldsymbol{\Theta}^i \boldsymbol{r}_{ij}}{\left\|\boldsymbol{r}_{ij}\right\|^5} \right) \tag{2}$$

We project electric fields across a bond vector from atom j to atom m (denoted as the $j-m$ bond) by scaling the average electric field by the normalized vector between the two bonded atoms (eq 3).

$$E^{\text{proj}}{}_{j-m} = (1/2) \times \frac{\boldsymbol{r}_m - \boldsymbol{r}_j}{\left\|\boldsymbol{r}_m - \boldsymbol{r}_j\right\|} \cdot (\boldsymbol{E}_j + \boldsymbol{E}_m) \tag{3}$$

Positive electric fields and positive dipole moments are both oriented toward positive charges, reflecting the direction a negative point charge would move (Supporting Information Figure S2). The electrostatic interaction energy is favorable when a dipole and electric field are oppositely oriented, or, equivalently, when cationic atoms are at lower electrostatic potentials than anionic atoms (Supporting Information Text S2).

3. COMPUTATIONAL DETAILS

3.1. Classical Molecular Dynamics

Topology and coordinate files for the molecular dynamics (MD) simulations were prepared using the ParmEd and tleap utilities in AMBER.[74] Acetone was parametrized with the generalized AMBER force field (GAFF) and solvated in hexane, tetrahydrofuran (THF), dichloromethane (DCM), dimethyl sulfoxide (DMSO), and water in a solvent box with 20 Å of buffer. Solvent parameters from Caleman et al. were used for THF, DMSO, hexane, and DCM,[75] and the TIP3P model was used for water.[76] MD was performed on homogeneous solvent and solvated acetone systems. All MD simulations were performed with Amber24 using the GPU-accelerated particle mesh Ewald, PMEMD module.[77,78] Nonbonded interactions were cut off at 8 Å, yielding similar solvation structure as a longer-range cutoff (Supporting Information Figure S3).[79] Systems were equilibrated following a standard protocol, including a 2 fs time step with SHAKE applied to constrain all bonds involving hydrogen (Supporting Information Figure S4). A total of 2 ns of equilibration and 100 ns production dynamics were collected. For each simulation, 50 frames were selected from the production run at 2 ns intervals for a total of 50 snapshots. From these frames,

https://doi.org/10.1021/acs.jctc.6c00065
J. Chem. Theory Comput. XXXX, XXX, XXX−XXX

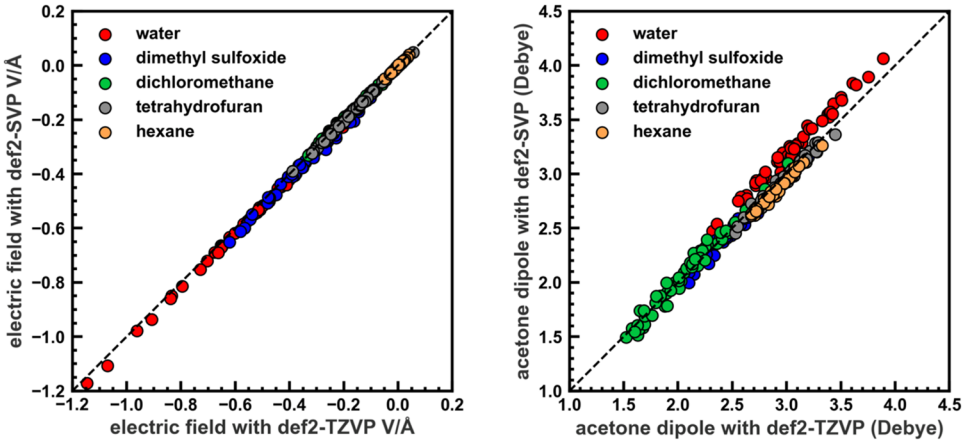

Figure 2. Comparison of electric fields across the O═C bond (left) and acetone dipole moments (right) computed from wave functions generated by QM single-point calculations with B3LYP/def2-SVP-D3 and B3LYP/def2-TZVP-D3. Electric fields and dipole moments were calculated with each wave function partitioned by the CM5 charge scheme. Each point indicates a frame in which a cluster of 7 Å solvent radius around an acetone solute molecule was extracted from the MD simulation.

CPPTraj was employed to select solvent molecules within 3, 5, 7, or 11 Å from the nearest solute atom to create QM clusters of increasing size.[80] In homogeneous (i.e., solute-free) solvent boxes, 14 Å diameter clusters were extracted and only the dipole moments of solvent molecules within 5 Å of the cluster center were included in the averaged total. Topology and parameter files are provided in the Zenodo repository.[81]

3.2. Quantum Mechanical Electric Field Calculations

Single-point quantum mechanical (QM) calculations were carried out using ORCA version 6.0.0[82] and a developer version of TeraChem 1.9.[83] We probed the influence of Hartree−Fock exchange and basis set identity on electric field calculations with different charge schemes. Here, we utilized a B3LYP[84−86] global hybrid functional with an empirical D3 dispersion correction[87] that employed Becke−Johnson damping.[88] We carried out calculations with modified Hartree−Fock (HF) exchange fractions (0.0 to 0.40 in 0.02 increments) and def2-SVP, def2-TZVP, def2-TZVPP, and def2-TZVPD basis sets (Supporting Information Table S1 and Text S3).[89] Clusters extracted from MD simulations were solvated with implicit solvent with dielectric constants of 7.58 for THF, 8.93 for DCM, and 78.4 for water, 1.88 for *n*-hexane, and 46.7 for DMSO. In ORCA, we employed the conductor-like polarizable continuum model (C-PCM),[90,91] with the COSMO form of the dielectric screening factor without any outlying charge correction.[92] C-PCM was also employed in TeraChem calculations. Solute cavity radii were defined using Bondi radii scaled by a factor of 1.2.[93] Electric field calculations were carried out using pyEF and Multiwfn from converged wave functions in the Molden file format[71,72] or using built-in postprocessing methods within ORCA.

4. RESULTS AND DISCUSSION

4.1. Sensitivity of Electric Fields to QM Protocol

Because we compute electric fields, electrostatic potentials, and electrostatic stabilization energies from atom-centered charge populations and charge distributions obtained from QM calculations, it is essential to determine how sensitive these properties are to the chosen QM methodology. Due to sensitivity of distributed multipole analysis to the density partitioning method and underlying QM method,[94,95] we anticipate that the accuracy of electric fields computed from a multipole expansion will depend on both the initial QM method and the subsequent charge-partitioning scheme. To better understand how the choice of method influences the results, we evaluate the sensitivity of solvent-mediated electric fields and dipole moments to basis set and Hartree−Fock (HF) exchange across a diverse set of charge partitioning schemes. Here, we specifically consider real-space charge schemes since they generally show superior basis set stability,[67] and we also report population analysis methods as low-cost alternatives. Additional charge partitioning methods including ESP-based methods are also available directly in pyEF via Multiwfn, and other charge schemes, such as NBO partial charges, can be incorporated into the pyEF framework directly via user-provided input using the B-factor column of a PDB file.

The basis set strongly influences computational cost, with electronic structure calculations scaling at least as $O(N^3)$, where N is the number of basis functions, so we first examine the sensitivity of properties to basis set size. We quantify basis set dependence by comparing the deviation of electric fields between a modest def2-SVP basis set and the larger def2-TZVP basis set. We carry out this analysis on a range of solvent clusters, where the cluster consists of all solvent molecules within 7 Å of an acetone solute molecule. We then compute electric fields arising from the solvent along the O═C bond vector of acetone. For these calculations, only nonsolute atoms are included in the many-body summation. We anticipate that basis set sensitivity will depend on the partial charge scheme, as observed in prior work.[96−99] Consistent with previous evidence, electric fields computed with Mulliken or Löwdin charges show high basis set dependence both in polar and nonpolar solvents (Supporting Information Figure S5 and Tables S2−S4). In water, electric fields computed with def2-SVP have mean absolute deviations (MADs) of 0.35 V/Å when computed with Mulliken charges and 0.172 V/Å when computed with Löwdin charges with respect to the def2-TZVP basis. Even in a nonpolar solvent such as DCM, MADs are as large as 0.076 V/Å for Mulliken and 0.207 V/Å for Löwdin (Supporting Information Figure S5 and Tables S2−S4). Since real-space derived partial charges are expected to be more robust to basis set size, we considered them next.

https://doi.org/10.1021/acs.jctc.6c00065
J. Chem. Theory Comput. XXXX, XXX, XXX−XXX

As expected, real-space methods including Hirshfeld, Hirshfeld-I, CM5, and Voronoi, are more robust to basis set size and consistently display good agreement between electric fields computed with def2-SVP and def2-TZVP basis sets, with MADs below 0.023 V/Å for the smaller basis set (Figure 2 and Supporting Information Figure S5). The density-corrected Hirshfeld (ADCH) scheme shows poorer results (mean average error of 0.067 V/Å) in water. Among all charge schemes, the CM5 scheme shows the greatest insensitivity to basis set with MADs below 0.018 V/Å in all solvents (Figure 2 and Supporting Information Tables S2−S4). Configurations with the highest basis set dependence in Hirshfeld, CM5, and Voronoi schemes tend to also show higher basis set dependence with the Hirshfeld-I population method (Supporting Information Figure S6). This correlation suggests that basis set sensitivities among real-space methods arise from basis-set-mediated changes in the molecular density, rather than the pro-molecular atomic weighting, which is varied in Hirshfeld-I but constant in Hirshfeld. In the rare snapshots where basis-set-mediated differences arise, there is no apparent correlation with the nature of the interaction between acetone and solvent.

We next considered the sensitivity of other properties to basis set choice. The dipole moments of the acetone solute, like electric fields computed with real-space charges, are relatively robust to basis set choice (Supporting Information Figure S7 and Tables S5−S7). For the more robust real-space partial charge schemes, dipole moments show the highest basis set disparity in water solvent where R^2 values are below 0.80 and deviations are above 5%. Although these dipole moments show highest basis set sensitivity in water, they are still relatively modest with real-space partial charge schemes. Across each solvent system, the CM5 charge scheme achieves the lowest mean absolute deviation between double- and triple-ζ basis sets, with differences remaining below 0.18 D (Supporting Information Table S6). Thus, effects of electrostatic environments are robust to basis set size, motivating smaller basis set selection to mitigate computational cost. However, in cases where it is necessary to achieve lower than 0.18 D accuracy in molecular dipole moments, a larger basis set is needed. To further reduce computational cost, it should be possible within the pyEF framework to implement a mixed-basis approach in which the solute is computed with a more extended basis set while the solvent is computed with a computationally efficient basis set. We will explore such an approach in future work.

We next evaluated the sensitivity of each charge scheme to the presence of polarization and diffuse functions in the basis sets. Among the most promising real-space charge schemes, addition of diffuse functions yields slight decreases in electric fields values (∼0.01 V/Å) and small but nonmonotonic changes in dipole moments (∼0.02 D, Supporting Information Figures S8−S9 and Tables S8−S9). While diffuse basis function effects are small, they are comparable to changes mediated by increasing basis set size from def2-SVP to def2-TZVP in nonpolar solvents (Supporting Information Table S6). Adding polarization functions has an even smaller, essentially negligible effect on properties computed from real-space charges in nonpolar solvents (Supporting Information Text S4 and Tables S10−S11). While basis set effects from polarization functions are expectedly larger in polar solvents such as water, they still influence dipoles by less than 0.03 D and decrease electric fields by 0.01 V/Å, corresponding to less than one-fifth of the associated changes from increasing the basis set size (i.e., def2-SVP to def2-TZVP). Notably, electric field and dipole values vary far more with solvent configuration than with the underlying force field or with changes in basis set (Supporting Information Figures S8−S10 and Text S5). Overall, real-space charge schemes demonstrate robustness with respect to basis set size, completeness and flexibility, which motivates the use of small basis sets in combination with real-space charges to reduce computational cost.

While real-space derived electric fields and dipole moments show limited but nonmonotonic sensitivity to basis set size, we observe a linear and monotonic increase in the magnitude of electric fields and acetone dipole moments with HF exchange (Supporting Information Figures S11−S13). Among the real-space schemes, the dipole moment of acetone is relatively insensitive to HF exchange in hexane but shows increasing sensitivity with solvent polarity (Supporting Information Figure S11). The largest sensitivities are observed in water, in which the Hirshfeld-I dipole moment of acetone changes by an average of 0.66 D when the HF exchange fraction is increased from 0.00 to 0.40. In comparison, changing the basis set from def-SVP to def2-TZVP yields an average change of only 0.19 D (Supporting Information Table S6). Acetone electric fields change linearly with HF exchange, with deviations from linearity falling below 0.0008 V/Å·HFX or less than 1% of the total value (Supporting Information Figure S14). In all but one case, the magnitude of real-space derived electric fields projected along the acetone O═C bond increases with HF exchange (Supporting Information Figures S15−S16 and Text S6).

We note that the systematic increase in magnitude of electrostatic properties with HF exchange tends to cancel when comparing chemical systems with a consistent HF exchange and thus has little impact on qualitative conclusions. Nevertheless, for quantitative agreement, it is necessary to select an appropriate HF fraction. Previous work reported that for first- and second-row atoms, iterative Hirshfeld charges computed from the global hybrid PBE0 wave function with HF exchange fractions of 0.25 and 0.33 show the best agreement with charges computed with the double hybrid revDSD-PBE86.[67] While higher HF exchange may be required to reflect electron localization in highly ionic systems,[100,101] we recommend HF exchange in the 0.25−0.33 range for primarily organic systems. Overall, we observe a linear increase in electric fields and dipole moments with HF exchange and demonstrate that real-space electrostatic parameters are only weakly dependent on both basis set size and HF exchange.

4.2. Cost−Accuracy Trade-Off in Partial Charge Schemes

To faithfully model electric fields in large molecular systems, an effective charge scheme should reproduce experimental observables at reasonable cost. Since partial charges are not experimental observables, we instead compare experimentally measured bulk solvent dipole moments with those computed with real-space charges at the center of a large solvent cluster (Figure 3). Overall, we observe that the dipole moments obtained from ADCH and CM5 charges closely match experimental dipole moments in hexane, THF, DCM, and DMSO, deviating by less than 0.13 and 0.10 D from experimental values. However, these charge schemes estimate liquid water dipole moments of 1.77 D on average, which is much closer to the gas-phase water dipole of 1.96 D than to the liquid-phase water dipole of 2.90 D (Supporting

https://doi.org/10.1021/acs.jctc.6c00065
J. Chem. Theory Comput. XXXX, XXX, XXX−XXX

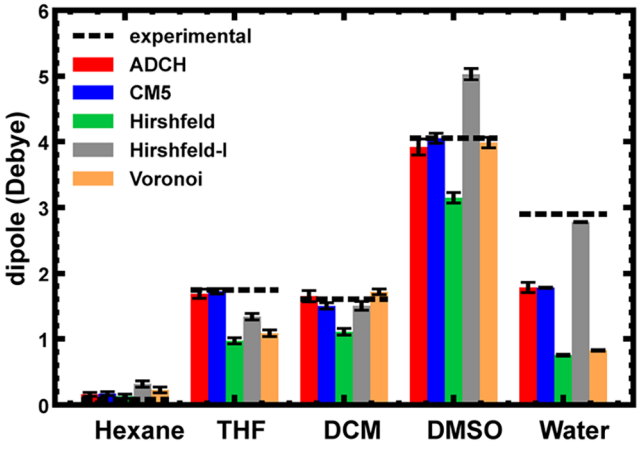

Figure 3. Average solvent dipole moments computed with five real-space partial charge schemes compared against experimental bulk solvent dipole moments (Supporting Information Table S12). Reported dipole values and standard deviations were computed from the cluster-wise averages.

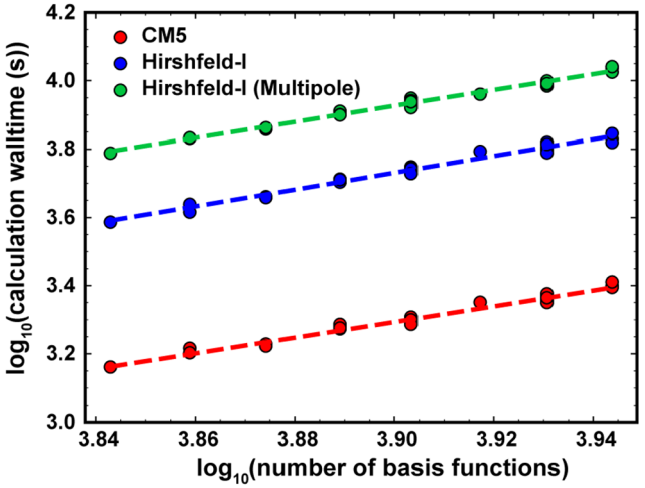

Figure 4. Scaling of computational cost for pyEF calculations with the number of basis functions for acetone solvated by a 7 Å shell of THF. Analysis is carried out after single-point DFT calculations with B3LYP/def2-TZVPD-D3. Calculations were run on 48 CPU cores of an Intel Xeon Platinum 8260 node. Walltime is measured from the beginning of a call to Multiwfn to completion of the Multiwfn calculation in pyEF.

Information Table S12). Only the Hirshfeld-I scheme provides a reasonable estimate of 2.78 D for the water dipole moment. This reflects the importance of self-consistent promolecular basins to capture the intermolecular polarization in the bulk for polar solvents such as water. This phenomenon is largely absent in the gas phase, but it arises from hydrogen bonding in the liquid phase.

Despite the better agreement of the water dipole moment computed with Hirshfeld-I charges to experiment, Hirshfeld-I struggles to capture the dipole moment of other polar solvents, overestimating the dipole moment of DMSO by 0.98 D while underestimating the dipole of THF by 0.40 D. The noniterative, Hirshfeld atomic charge scheme also performs poorly, consistently underestimating the dipole moments by as much as 2.14 D for water and 0.90 D for DMSO.[96] For both the Hirshfeld and iterative Hirshfeld schemes, we also considered the potential effect of higher-order terms on the evaluation of the dipole moment. As expected, we found negligible changes in predicted dipole moment when including higher-order terms in the multipole expansion, but we will consider multipole effects further in the context of electric field evaluations next (see Section 4.3 and Supporting Information Figure S17). Since the ADCH and CM5 methods provide the closest average approximation of experimental dipole moments in solvents besides water, we anticipate that they will most faithfully capture electrostatics in environments with limited intermolecular polarization. The iterative Hirshfeld scheme more accurately captures strong intermolecular polarization and thus should be applied to model systems with strong hydrogen bonding or dipole−dipole interactions.

We next assessed the relative cost−accuracy trade-off among real-space partial charge schemes. To do so, we quantified the scaling of computational cost (i.e., wall time of the pyEF calculation) with the number of basis functions for each real-space method for 30 geometries consisting of acetone with a 7-Å THF solvent shell (ranging from 348 to 439 atoms in total, Figure 4 and Supporting Information Table S13). Among all noniterative real-space methods including Hirshfeld and its variants (i.e., ADCH, CM5, and Voronoi as well), we observe scaling close to $O(N^{2.3})$ with comparable prefactors (ca. 3.37−3.64·10^{-3}) (Supporting Information Table S13). In contrast, the iterative Hirshfeld algorithm shows a steeper dependence on the number of basis functions $O(N^{2.45})$, leading to much longer wall times for larger systems (i.e., 7000 s vs 2573 s for 439 atoms or 8785 basis functions, Figure 4). The fuzzy-atom implementation of the iterative Hirshfeld algorithm, which we use to compute multipole moments, shows weaker scaling $O(N^{2.32})$ but a larger prefactor (5.67·10^{-3}) than other methods. This larger prefactor results in the highest cost in all cases we examine. Even in the smallest, 348-atom system, the iterative Hirshfeld scheme more than doubles total cost over a CM5 calculation (3852 s vs 1440 s, respectively), while the fuzzy-atom analysis quadruples the cost (6134 s) of pyEF analysis compared with the baseline CM5 method.

Above ∼12,000 basis functions, high stack memory requirements prohibit Hirshfeld-I calculations even when stack limits are lifted on an Intel Xeon Platinum 8260 node (Supporting Information Figure S18). To mitigate memory limitations, the pyEF code defaults to a slower, more memory efficient algorithm for Hirshfeld-I when the system is larger than 12,000 basis functions. This cutoff can be adjusted by the user to reflect limits of their computing architecture. Overall, we observe negligible benefit in dipole accuracy but high additional cost for the fuzzy-atom analysis and thus recommend applying monopole treatment. For most large systems, the CM5 scheme provides the best balance of cost and dipole accuracy, while iterative Hirshfeld may be worth the additional cost when systems are characterized by strong intermolecular polarization.

To contextualize the importance of selecting a suitable partial-charge scheme (i.e., CM5 or Hirshfeld-I) to compute electric fields, we computed acetone Stark tuning rates. Stark tuning rates are used to quantify the sensitivity of a vibrational mode to changes in local electric fields. Here, we quantify the Stark tuning rate for the C═O stretching mode of acetone by correlating acetone vibrational frequencies from literature experimental results with computationally predicted electric field projections across the O═C bond axis (Figure 5 and Supporting Information Table S14).[102] Among real-space

https://doi.org/10.1021/acs.jctc.6c00065
J. Chem. Theory Comput. XXXX, XXX, XXX−XXX

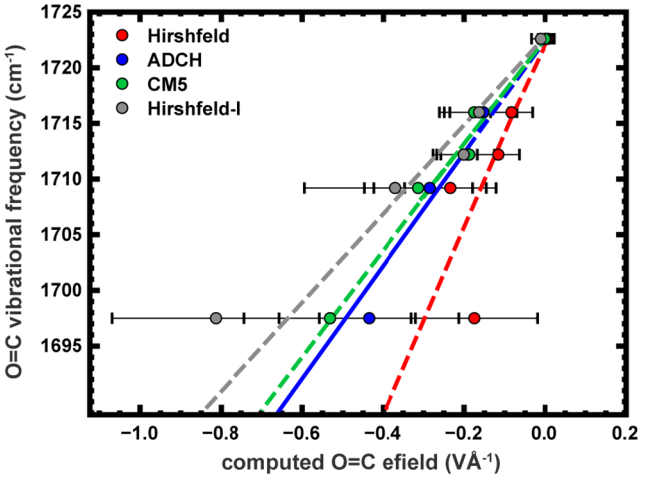

Figure 5. Average electric fields projected across the O═C acetone bond in 7 Å of solvent plotted as a function of the experimental vibrational frequency of the O═C stretching mode in each solvent (listed left to right): water, DMSO, DCM, THF, hexane. Each point indicates the average electric field across 50 snapshots, and the error bars indicate the standard deviation among samples. pyEF was applied after converging wave functions for each geometry at B3LYP-D3/def2-TZVP level of theory. Dashed lines indicate the linear regression accounting for all 50 samples in each solvent.

methods, we observe the lowest Stark tuning rate of 39.85 ± 0.2 cm^{-1}/V/Å with the iterative Hirshfeld approach (Supporting Information Table S14). Even without the computationally demanding, self-consistent promolecule refinement of Hirshfeld-I charges, CM5 and ADCH partial charge schemes predict comparable Stark tuning rates (46.97 ± 0.2 cm^{-1}/ V/Å and 50.73 ± 0.3 cm^{-1}/ V/Å, respectively). Notably, these values lie within the range of 37 to 74 cm^{-1}/ V/Å estimated from frozen glass experiments with local field factors ranging from two to one.[103] Previous analysis with only MD-level partial charges estimated a stark tuning rate of 31 cm^{-1}/ V/Å, below the range estimated from experiment.[103] While Stark tuning rates are highly dependent on the partial-charge scheme, they are relatively insensitive to basis set. The tuning rates change by less than 1% between def2-TZVP and def2-SVP for each real-space partial charge method (Supporting Information Table S14). Based on benchmarks for partial-charge-derived dipole moments against experimental values, as well as agreement with the range defined from frozen glass experiments, we expect that the CM5, ADCH, and Hirshfeld-I partial charge schemes should provide the most faithful estimates of Stark tuning rates.

4.3. Incorporating Long-Range Electrostatics

After establishing the sensitivity to basis set and DFT method as well as charge partitioning schemes for computing atom-wise electric fields, we next evaluated how the solvent cluster model size influences these calculations. Specifically, we quantified the electric field aligned with the O═C bond of acetone when solvated with hexane, THF, DCM, DMSO, and water using shells of explicit solvent molecules within radii of 3 Å, 5 Å, 7 Å, and 11 Å of the nearest acetone atom (see Section 3.1). This increase in solvent shell corresponds with a steep increase in atom count: water clusters with a 5 Å solvation shell around acetone contain an average of 130 atoms (ca. 40 water molecules), whereas clusters with an 11 Å radius include about 889 atoms (ca. 293 water molecules) (Supporting Information Figure S19). As solvent shells increase from 3 Å to 7 Å, real-space electric field values monotonically converge toward those obtained with the 11 Å shell (Figure 6 and Supporting

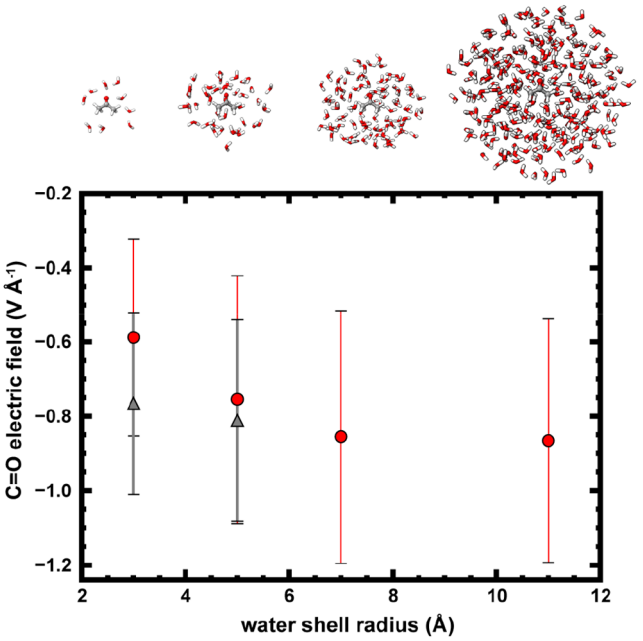

Figure 6. Average O═C electric field across a set of 10 clusters with radii of 3, 5, 7, and 11 Å of water surrounding acetone computed with B3LYP-D3/def2-SVP. Electric field contributions from atoms in the QM region were computed with the Hirshfeld-I scheme. Red circles indicate electric fields were calculated from QM clusters only while gray triangles indicate both QM clusters and surrounding MM point charges were included in electric field calculation. MM point charges include atoms excluded from QM region but within 20 Å of solvent padding around the acetone solute.

Information Figure S20 and Tables S15−S17). Among the solvent clusters, O═C electric fields in THF clusters are most sensitive to the shell radius, with deviations from the 11-Å solvent shell reference decreasing from 130% (0.0545 V/Å) with a 3-Å solvent shell, to 60% (0.0406 V/Å) with a 5-Å solvent shell, to 46% (0.0226 V/Å) with a 7-Å solvent shell (Supporting Information Figures S21−S22). In water, we observe large absolute changes in electric fields with cluster size, where increasing clusters of 3-Å, 5-Å, and 7-Å solvent radius exhibit differences from the 11-Å solvent cluster radius corresponding to 32% (0.2773 V/Å), 14% (0.1137 V/Å), and 11% (0.0859 V/Å). Even in the 7-Å shell, electric fields among all solvents deviate by more than 10% from the value in the 11-Å shell. These results suggest that electrostatic effects of solvation by both nonpolar and polar solvents require more than 7 Å of solvation to account for 90% of the electric field produced by two full solvent shells (i.e., ∼11 Å).

To mitigate the high computational cost associated with the large solvation shells required to fully capture the electric field at the acetone solute, we repeated the above analysis now combining high-quality QM-derived partial charges to represent local interactions with MM-derived point charges to model long-range electrostatics. After converging the wave function using electrostatic QM/MM embedding, the resulting QM region was partitioned using the Hirshfeld-I, ADCH, or CM5 schemes, and these partial charges were combined with contributions from the MM point charges. We quantified the

https://doi.org/10.1021/acs.jctc.6c00065
J. Chem. Theory Comput. XXXX, XXX, XXX−XXX

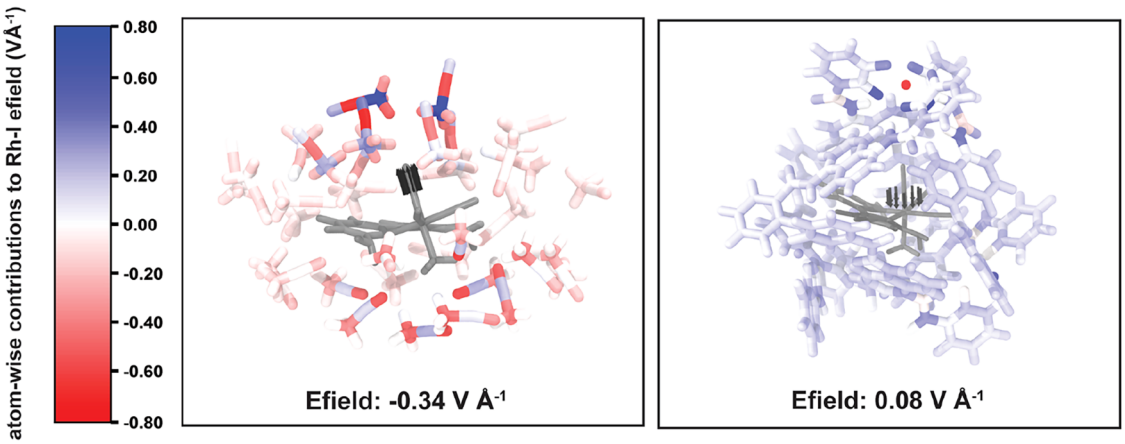

Figure 7. Visualization of (Rh(III)$(CO)_2(NH_2)_2$bpy)-MeI (CSD refcode: AXEDEN) transition metal complex in acetonitrile (left) and within a $Ga_4L_6^{12-}$ cage on right. AXEDEN-MeI is depicted by gray sticks and the electric field across the I−Rh bond is shown as field lines with magnitude and direction proportional to the computed value. Solvent and cage atoms are colored by their relative contribution to the I−Rh electric field, with positive contributions indicated in blue and negative contributions indicated with red. All atomic contributions for both structures are colored by same relative scale.

electric fields for solvated systems partitioned into QM regions of 3 Å and 5 Å about the solute within a 20-Å shell of MM point charges and compared these results to fields obtained from an 11-Å, fully quantum-mechanical solvation shell. The QM/MM model applying Hirshfeld-I for the 5-Å QM region showed improved agreement with the 11-Å reference, yielding mean deviations of 0.01−0.08 V/Å or 7% to 42% (Figure 6 and Supporting Information Figures S21−S22). Overall, the QM/MM model with a 5-Å QM region has a lower frame-wise average deviation than the 7-Å QM-only model, with a nearly 4-fold reduction in computational cost (Supporting Information Figure S23). Decreasing the size of the QM region to 3 Å in QM/MM decreases performance in all cases but still shows more than a 4% improvement over the 5-Å QM cluster in THF, DCM, and water at less than a fifth of the computational cost of the 5-Å QM cluster (Supporting Information Figure S23). In highly polar environments, it may be necessary to incorporate polarization of MM point charges by the QM region, and, for such cases, pyEF supports linear polarization of MM region (Supporting Information Text S7). In highly charged or polar environments, it may be necessary to model the MM region with a polarizable force field to sufficiently capture inductive effects and faithfully model dynamics. Future efforts will incorporate multipole moments from the AMOEBA polarizable force field[104] to both the QM/MM interface and for a purely MM based electric field analysis. Overall, these results indicate that in organic environments, long-range effects on electric fields can be approximated to within 0.08 V/Å when atoms beyond ∼5 Å from the solute are represented using fixed point charges, offering substantial computational savings relative to full QM treatment.

4.4. Case Study on the Effect of Chemical Environments on Electric Fields

To demonstrate how pyEF can be used to study the mechanisms of electrostatic preorganization in catalysis, we evaluated electric fields projected onto metal−ligand bonds of a previously studied trialkylphosphine dimethyl gold transition metal complex to compare with prior work and a representative catalyst both bound in a $Ga_4L_6^{12-}$ nanocage (Supporting Information Figures S24−S25 and Tables S18−S19).[45] Leveraging QM/MM methodology and modest basis sets, we examine the electric field on the iodide ligand of a dicarbonyl(6,6′-diamino- [2,2′-bipyridyl])MeI rhodium complex. Addition of iodide and methyl ligands is the rate-limiting step in the carbonylation reaction over Rh(I)-$(CO)_2(NH_2)_2$bpy, which was previously shown[105] with computational modeling to bind favorably in the $Ga_4L_6^{12-}$ cage (Supporting Information Figure S25). Although the full cage system contains 280 atoms, we combine observations from the preceding sections to select a standard B3LYP functional in combination with a modest double-ζ basis set and effective core potential (ECP, i.e., def2-SVP with def2-ECP)[106] along with Hirshfeld-I charges to robustly partition the electron density without sacrificing fidelity. To evaluate the role of encapsulation, we compare the (Rh(III)-$(CO)_2(NH_2)_2$bpy)MeI complex bound within the $Ga_4L_6^{12-}$ cage and explicitly solvated with a 5-Å shell of QM acetonitrile further surrounded by QM/MM embedding of 20 Å. In the absence of the cage, the acetonitrile solvent exerts an electric field of −0.34 V/Å across the I−Rh bond, leading to an elongated 3.14 Å I−Rh bond length (Figure 7 and Supporting Information Table S19). When encapsulated in the cage, nitrogen and oxygen atoms on the carbonyl linkers screen the positive charge on the closest gallium node (shown in bright red in Figure 7). The combined effect of the cage exerts an electric field of 0.08 V/Å and stabilizes a shortened I−Rh bond length of 2.88 Å (Figure 7 and Supporting Information Table S19). By decomposing the cage-mediated electric field, we find that polar substituents on cage linkers rather than the highly charged gallium nodes determine the orientation of the field within the cage. This observation suggests that linker functionalization provides the most promising path to control electrostatics in this cage microenvironment. This case study highlights how pyEF may be used to efficiently decompose electrostatic effects to further enable rational design of supramolecular interactions.

5. CONCLUSIONS

In this work, we introduced pyEF, a Python package for computing electrostatic properties in molecular systems. The pyEF code accepts Molden files generated by many quantum chemistry software packages and interfaces with Multiwfn to

https://doi.org/10.1021/acs.jctc.6c00065
J. Chem. Theory Comput. XXXX, XXX, XXX−XXX

automatically partition the QM electron density into atom-centered monopole or multipole moments. These multipole moments, together with any additional MM point charges, are combined to yield atom-decomposable electric fields, electrostatic interaction energies, and electrostatic potentials.

Using pyEF, we probed the sensitivity of electric field calculations to the QM method, QM region size, and charge partitioning scheme. Electric fields calculated with real-space partitioning methods were largely stable with respect to basis set size. However, electric field values were very dependent on the charge partitioning method, such that acetone Stark tuning rates varied two-fold depending on the approach used. By comparing experimental solvent dipole moments with those obtained from each real-space method, we determined that only the CM5, ADCH, and Hirshfeld-I schemes reliably reproduced liquid-phase dipole moments, with water best described by Hirshfeld-I but the other solvents slightly better described by CM5 or ADCH. These real-space partial charge methods thus provided the most trustworthy foundation for electric field and Stark tuning rate calculations in similar systems. To further reduce the cost of both the initial QM calculations and the subsequent pyEF postprocessing, we replaced distant molecules with MM point charges and assessed the convergence of electric field calculations with respect to QM region size in QM/MM. In homogeneous solvents, we found that contributions from the second solvation shell to the electric field experienced by the solute could be reasonably approximated using MM point charges.

Finally, we demonstrated that pyEF could be employed in a large catalytic system to elucidate the molecular origin of strong electric fields. While further work is needed to incorporate higher-order terms in the MM region of QM/MM simulations and understand electric fields in systems with strong electron correlation or unpaired electrons, we anticipate this framework may be useful to inform the design of electrostatic preorganization in supramolecular systems.

■ ASSOCIATED CONTENT

Data Availability Statement

Amber topology and parameter files for all systems studied, processing scripts for cluster and QM/MM extractions, ORCA input scripts, pyEF input scripts for each calculation type as well as a copy of the pyEF code at the time of preparation of this manuscript are provided in the Zenodo repository: 10.5281/zenodo.15529327.[81]

Supporting Information

The Supporting Information is available free of charge at https://pubs.acs.org/doi/10.1021/acs.jctc.6c00065.

Schematic of software workflow; information on electrostatic sign conventions; mathematic details on calculation of electrostatic energy; details on solvent structure around acetone solute; additional plots detailing electric field and dipole moment dependence on Fock exchange, basis set size, and incorporation of diffuse and polarization functions into basis set; information on computational cost of electrostatic calculations; comparison of acetone Stark tuning rates by partial charge method; tabulation of electric field values across acetone O=C bond with changes in QM/MM cluster size with different partial charge methods. Additional details on the transition metal complex demonstration system, including mechanism and tabulation of key electrostatics and associated bond lengths in solvent and Gallium nanocage environment (PDF)

■ AUTHOR INFORMATION

Corresponding Author

Heather J. Kulik − *Department of Chemical Engineering, Massachusetts Institute of Technology, Cambridge, Massachusetts 02139, United States; Department of Chemistry, Massachusetts Institute of Technology, Cambridge, Massachusetts 02139, United States;* orcid.org/0000-0001-9342-0191; Email: hjkulik@mit.edu

Authors

Melissa T. Manetsch − *Department of Chemical Engineering, Massachusetts Institute of Technology, Cambridge, Massachusetts 02139, United States;* orcid.org/0000-0003-3721-6131

David W. Kastner − *Department of Chemical Engineering, Massachusetts Institute of Technology, Cambridge, Massachusetts 02139, United States; Department of Bioengineering, Massachusetts Institute of Technology, Cambridge, Massachusetts 02139, United States;* orcid.org/0000-0002-7766-4249

Yuriy Román-Leshkov − *Department of Chemical Engineering, Massachusetts Institute of Technology, Cambridge, Massachusetts 02139, United States; Department of Chemistry, Massachusetts Institute of Technology, Cambridge, Massachusetts 02139, United States;* orcid.org/0000-0002-0025-4233

Complete contact information is available at: https://pubs.acs.org/10.1021/acs.jctc.6c00065

Notes

The authors declare no competing financial interest.

■ ACKNOWLEDGMENTS

This work was supported by the U.S. Department of Energy, Office of Science, Office of Advanced Scientific Computing, Office of Basic Energy Sciences, via the Scientific Discovery through Advanced Computing (SciDAC) program (to M.T.M. and H.J.K.) and U.S. Department of Energy, Office of Basic Energy Sciences under Award No. DE-SC0016214 (to M.T.M. and Y.R.-L.). This work was partially supported by the National Institute of General Medical Sciences of the National Institutes of Health under award number R35GM152027 (to H.J.K. and D.W.K.). Partial support was provided by National Science Foundation Graduate Research Fellowships under Grant #1745302 for M.T.M. and D.W.K. The authors acknowledge the MIT SuperCloud and Lincoln Laboratory for providing HPC resources and Expanse at San Diego Supercomputer Center through allocation CHE140073 from the Advanced Cyberinfrastructure Coordination Ecosystem: Services & Support (ACCESS) program, which is supported by National Science Foundation grants #2138259, #2138286, #2138307, #2137603, and #2138296. The authors thank Adam H. Steeves for providing a critical reading of the manuscript and Husain Adamji, Clorice Reinhardt, Bhavish Dinakar, and Karl Westendorff for scientific discussion.

■ REFERENCES

(1) Warshel, A.; Levitt, M. Theoretical studies of enzymic reactions: Dielectric, electrostatic and steric stabilization of the carbonium ion in

the reaction of lysozyme. *J. Mol. Biol.* **1976**, *103* (2), 227−249, DOI: 10.1016/0022-2836(76)90311-9.
(2) Warshel, A.; Sharma, P. K.; Kato, M.; Xiang, Y.; Liu, H.; Olsson, M. H. M. Electrostatic Basis for Enzyme Catalysis. *Chem. Rev.* **2006**, *106*, 3210−3235.
(3) Fried, D. F.; Bagchi, S.; Boxer, S. G. Extreme Electric Field Powers Catalysis in the Active Stie of Ketosteroid Isomerase. *Science* **2014**, *346*, 1510−1513.
(4) Chaturvedi, S. S.; Goswami, A.; Qian, J.; Petersen, A.; Ajmera, P.; Alexandrova, A. N. Distinct Electric Fields Enable Common Catalytic Function in Structurally Diverse Enzymes. *J. Am. Chem. Soc.* **2025**, *147*, 32225−32237.
(5) Azcarate, I.; Costentin, C.; Robert, M.; Saveant, J. M. Through-Space Charge Interaction Substituent Effects in Molecular Catalysis Leading to the Design of the Most Efficient Catalyst of Co(2)-to-Co Electrochemical Conversion. *J. Am. Chem. Soc.* **2016**, *138*, 16639−16644.
(6) Wesley, T. S.; Román-Leshkov, Y.; Surendranath, Y. Spontaneous Electric Fields Play a Key Role in Thermochemical Catalysis at Metal-Liquid Interfaces. *ACS Cent. Sci.* **2021**, *7*, 1045−1055.
(7) Xiong, H.; Lee, J. K.; Zare, R. N.; Min, W. Strong Electric Field Observed at the Interface of Aqueous Microdroplets. *J. Phys. Chem. Lett.* **2020**, *11*, 7423−7428.
(8) Shi, L.; LaCour, R. A.; Qian, N.; Heindel, J. P.; Lang, X.; Zhao, R.; Head-Gordon, T.; Min, W. Water Structure and Electric Fields at the Interface of Oil Droplets. *Nature* **2025**, *640*, 87−93.
(9) Zheng, C.; Ji, Z.; Mathews, I. I.; Boxer, S. G. Enhanced Active-Site Electric Field Accelerates Enzyme Catalysis. *Nat. Chem.* **2023**, *15*, 1715−1721.
(10) Bofill, J. M.; Quapp, W.; Albareda, G.; Moreira, I. P. R.; Ribas-Arino, J. Controlling Chemical Reactivity with Optimally Oriented Electric Fields: A Generalization of the Newton Trajectory Method. *J. Chem. Theory Comput* **2022**, *18*, 935−952.
(11) Bofill, J. M.; Severi, M.; Quapp, W.; Ribas-Arino, J.; Moreira, I. P. R.; Albareda, G. An Algorithm to Find the Optimal Oriented External Electrostatic Field for Annihilating a Reaction Barrier in a Polarizable Molecular System. *J. Chem. Phys.* **2023**, *159*, No. 114112, DOI: 10.1063/5.0167749.
(12) Singh, P.; Li, Q.; Liu, Y.; Che, F. Multiscale Simulation Guided Electric Field-Enhanced Ammonia Catalytic Cracking. *ACS Catal.* **2025**, *15*, 7690−7699.
(13) Siddiqui, S. A.; Stuyver, T.; Shaik, S.; Dubey, K. D. Designed Local Electric Fields-Promising Tools for Enzyme Engineering. *JACS Au* **2023**, *3*, 3259−3269.
(14) Welborn, V. V.; Ruiz Pestana, L.; Head-Gordon, T. *Nature Catalysis*; Nature Publishing Group, 2018; Vol. *1*.
(15) Aragonès, A. C.; Haworth, N. L.; Darwish, N.; Ciampi, S.; Bloomfield, N. J.; Wallace, G. G.; Diez-Perez, I.; Coote, M. L. Electrostatic Catalysis of a Diels-Alder Reaction. *Nature* **2016**, *531*, 88−91.
(16) Wang, Z.; Danovich, D.; Ramanan, R.; Shaik, S. Oriented-External Electric Fields Create Absolute Enantioselectivity in Diels-Alder Reactions: Importance of the Molecular Dipole Moment. *J. Am. Chem. Soc.* **2018**, *140*, 13350−13359.
(17) Mattioli, E. J.; Bottoni, A.; Zerbetto, F.; Calvaresi, M. Oriented External Electric Fields Affect Rate and Stereoselectivity of Electrocyclic Reactions. *J. Phys. Chem. C* **2019**, *123*, 26370−26378.
(18) Gorin, C. F.; Beh, E. S.; Kanan, M. W. An Electric Field-Induced Change in the Selectivity of a Metal Oxide-Catalyzed Epoxide Rearrangement. *J. Am. Chem. Soc.* **2012**, *134*, 186−189.
(19) Zhang, L.; Laborda, E.; Darwish, N.; Noble, B. B.; Tyrell, J. H.; Pluczyk, S.; Le Brun, A. P.; Wallace, G. G.; Gonzalez, J.; Coote, M. L.; Ciampi, S. Electrochemical and Electrostatic Cleavage of Alkoxyamines. *J. Am. Chem. Soc.* **2018**, *140*, 766−774.
(20) Dutta Dubey, K.; Stuyver, T.; Kalita, S.; Shaik, S. Solvent Organization and Rate Regulation of a Menshutkin Reaction by Oriented External Electric Fields Are Revealed by Combined Md and Qm/Mm Calculations. *J. Am. Chem. Soc.* **2020**, *142*, 9955−9965.
(21) Tang, C.; Su, M.; Lu, T.; Zheng, J.; Wang, J.; Zhou, Y.; Zou, Y. L.; Liu, W.; Huang, R.; Xu, W.; Chen, L.; Zhang, Y.; Bai, J.; Yang, Y.; Shi, J.; Liu, J.; Hong, W. Massive Acceleration of S(N)2 Reaction Using the Oriented External Electric Field. *Chem. Sci.* **2024**, *15*, 13486−13494.
(22) Dinakar, B.; Westendorff, K. S.; Torres, J. F.; Dakhchoune, M.; Groenhout, K.; Ewell, N.; Surendranath, Y.; Dinca, M.; Roman-Leshkov, Y. Elucidating Electric Field-Induced Rate Promotion of Bronsted Acid-Catalyzed Alcohol Dehydration. *J. Am. Chem. Soc.* **2025**, *147*, 27599−27610.
(23) Westendorff, K. S.; H, M. J.; Wesley, T. S.; Román-Leshkov, Y.; Surendranath, Y. Electrically Driven Proton Transfer Promotes Brønsted Acid Catalysis by Orders of Magnitude. *Science* **2024**, *383*, 757−763.
(24) Andrews, S. S.; Boxer, S. G. Vibrational Stark Effects of Nitriles Ii. Physical Origins of Stark Effects from Experiment and Perturbation Models. *J. Phys. Chem. A* **2002**, *106*, 469−477.
(25) Fried, S. D.; Boxer, S. G. Measuring Electric Fields and Noncovalent Interactions Using the Vibrational Stark Effect. *Acc. Chem. Res.* **2015**, *48*, 998−1006.
(26) Sorenson, S. A.; Patrow, J. G.; Dawlaty, J. M. Solvation Reaction Field at the Interface Measured by Vibrational Sum Frequency Generation Spectroscopy. *J. Am. Chem. Soc.* **2017**, *139*, 2369−2378.
(27) Fafarman, A. T.; Sigala, P. A.; Herschlag, D.; Boxer, S. G. Decomposition of Vibrational Shifts of Nitriles into Electrostatic and Hydrogen-Bonding Effects. *J. Am. Chem. Soc.* **2010**, *132*, 12811−12813.
(28) Kohler, B. E.; Woehl, J. C. Measuring Internal Electric Fields with Atomic Resolution. *J. Chem. Phys.* **1995**, *102*, 7773−7781.
(29) Andrews, S. S.; Boxer, S. G. Vibrational Stark Effects of Nitriles. I. Methods and Experimental Results. *J. Phys. Chem. A* **2000**, *104*, 11853−11863.
(30) Lake, W. R.; Meng, J.; Dawlaty, J. M.; Lian, T.; Hammes-Schiffer, S. Electro-Inductive Effect Dominates Vibrational Frequency Shifts of Conjugated Probes on Gold Electrodes. *J. Am. Chem. Soc.* **2023**, *145*, 22548−22554.
(31) Verma, N.; Tao, Y.; Zou, W.; Chen, X.; Chen, X.; Freindorf, M.; Kraka, E. A Critical Evaluation of Vibrational Stark Effect (Vse) Probes with the Local Vibrational Mode Theory. *Sensors* **2020**, *20*, No. 2358, DOI: 10.3390/s20082358.
(32) Bradshaw, R. T.; Dziedzic, J.; Skylaris, C. K.; Essex, J. W. The Role of Electrostatics in Enzymes: Do Biomolecular Force Fields Reflect Protein Electric Fields? *J. Chem. Inf. Model.* **2020**, *60*, 3131−3144.
(33) Kirsh, J. M.; Weaver, J. B.; Boxer, S. G.; Kozuch, J. Critical Evaluation of Polarizable and Nonpolarizable Force Fields for Proteins Using Experimentally Derived Nitrile Electric Fields. *J. Am. Chem. Soc.* **2024**, *146*, 6983−6991.
(34) Welborn, V. V.; Head-Gordon, T. Fluctuations of Electric Fields in the Active Site of the Enzyme Ketosteroid Isomerase. *J. Am. Chem. Soc.* **2019**, *141*, 12487−12492.
(35) Suydam, I. T.; S, C. D.; Pande, V. S.; Boxer, S. G. Electric Fields at the Active Site of an Enzyme: Direct Comparison of Experiment with Theory. *Science* **2006**, *313* (5784), 200−204, DOI: 10.1126/science.1127159.
(36) Di Pino, S.; Banerjee, D.; Monti, M.; Miron, G. D.; Cassone, G.; Hassanali, A. Deconstructing the Origins of Interfacial Catalysis: Why Electric Fields Are Inseparable from Solvation. *J. Chem. Phys.* **2025**, *163*, No. 184505, DOI: 10.1063/5.0288327.
(37) Fried, S. D.; Bagchi, S.; Boxer, S. G. Measuring Electrostatic Fields in Both Hydrogen-Bonding and Non-Hydrogen-Bonding Environments Using Carbonyl Vibrational Probes. *J. Am. Chem. Soc.* **2013**, *135*, 11181−11192.
(38) Ponder, P. R.; Ponder, J. W. Polarizable Atomic Multipole Water Model for Molecular Mechanics Simulation. *J. Phys. Chem. B* **2003**, *107*, 5933−5947.

(39) Nash, J.; Barnes, T.; Welborn, V. Electric: Electric Fields Leveraged from Multipole Expansion Calculations in Tinker Rapid Interface Code. *J. Open Source Software* **2020**, *5*, 2576.
(40) Polêto, M. D.; Lemkul, J. A. Tupã: Electric Field Analyses for Molecular Simulations. *J. Comput. Chem.* **2022**, *43*, 1113−1119.
(41) Ajmera, P.; Vargas, S.; Chaturvedi, S. S.; Hennefarth, M.; Alexandrova, A. N. Pycpet Horizontal Line Computing Heterogeneous 3d Protein Electric Fields and Their Dynamics. *J. Chem. Theory Comput* **2025**, *21*, 4299−4308.
(42) Wang, X.; Liu, H.; Li, Y.; Li, J.; Li, W. L. Tinkermodeller: An Efficient Tool for Building Biological Systems in Tinker Simulations. *J. Chem. Theory Comput* **2025**, *21*, 2712−2722.
(43) Kozuch, J.; Schneider, S. H.; Zheng, C.; Ji, Z.; Bradshaw, R. T.; Boxer, S. G. Testing the Limitations of Md-Based Local Electric Fields Using the Vibrational Stark Effect in Solution: Penicillin G as a Test Case. *J. Phys. Chem. B* **2021**, *125*, 4415−4427.
(44) Bhowmick, A.; Sharma, S. C.; Head-Gordon, T. The Importance of the Scaffold for De Novo Enzymes: A Case Study with Kemp Eliminase. *J. Am. Chem. Soc.* **2017**, *139*, 5793−5800.
(45) Welborn, V. V.; Li, W. L.; Head-Gordon, T. Interplay of Water and a Supramolecular Capsule for Catalysis of Reductive Elimination Reaction from Gold. *Nat. Commun.* **2020**, *11* (1), No. 415.
(46) Zhao, S.; Gong, K.; Song, Z.; Cassone, G.; Xie, J. Exploring the Linear Energy Relationships between Activation Energy and Reaction Energy under an Electric Field. *J. Chem. Theory Comput.* **2025**, *21*, 4615−4625.
(47) Zhang, P.; Xu, X. Modulation of Electric Field and Interface on Competitive Reaction Mechanisms. *J. Chem. Theory Comput.* **2025**, *21*, 6584−6593.
(48) Wang, L.; Fried, S. D.; Markland, T. E. Proton Network Flexibility Enables Robustness and Large Electric Fields in the Ketosteroid Isomerase Active Site. *J. Phys. Chem. B* **2017**, *121*, 9807−9815.
(49) Błasiak, B.; Cho, M. Vibrational Solvatochromism. Iii. Rigorous Treatment of the Dispersion Interaction Contribution. *J. Chem. Phys.* **2015**, *143*, No. 164111.
(50) Błasiak, B.; Londergan, C. H.; Webb, L. J.; Cho, M. Vibrational Probes: From Small Molecule Solvatochromism Theory and Experiments to Applications in Complex Systems. *Acc. Chem. Res.* **2017**, *50*, 968−976.
(51) Zheng, C.; Mao, Y.; Markland, T. E.; Boxer, S. G. Beyond the Vibrational Stark Effect: Unraveling the Large Redshifts of Alkyne C-H Bond in Solvation Environments. *J. Am. Chem. Soc.* **2025**, *147*, 6227−6235.
(52) Gao, A.; Remsing, R. C. Self-Consistent Determination of Long-Range Electrostatics in Neural Network Potentials. *Nat. Commun.* **2022**, *13*, No. 1572, DOI: 10.1038/s41467-022-29243-2.
(53) Eberhart, M. E.; Alexandrova, A. N.; Ajmera, P.; Bim, D.; Chaturvedi, S. S.; Vargas, S.; Wilson, T. R. Methods for Theoretical Treatment of Local Fields in Proteins and Enzymes. *Chem. Rev.* **2025**, *125*, 3772−3813.
(54) Pérez-Barcia, Á.; Cardenas, G.; Nogueira, J. J.; Mandado, M. Effect of the Qm Size, Basis Set, and Polarization on Qm/Mm Interaction Energy Decomposition Analysis. *J. Chem. Inf. Model.* **2023**, *63*, 882−897.
(55) Karelina, M.; Kulik, H. J. Systematic Quantum Mechanical Region Determination in Qm/Mm Simulation. *J. Chem. Theory Comput.* **2017**, *13*, 563−576.
(56) Kulik, H. J.; Zhang, J.; Klinman, J. P.; Martínez, T. J. How Large Should the Qm Region Be in Qm/Mm Calculations? The Case of Catechol O-Methyltransferase. *J. Phys. Chem. B* **2016**, *120*, 11381−11394.
(57) Mehmood, R.; Kulik, H. J. Both Configuration and Qm Region Size Matter: Zinc Stability in Qm/Mm Models of DNA Methyltransferase. *J. Chem. Theory Comput.* **2020**, *16*, 3121−3134.
(58) Wang, X.; He, X. An Ab Initio Qm/Mm Study of the Electrostatic Contribution to Catalysis in the Active Site of Ketosteroid Isomerase. *Molecules* **2018**, *23*, No. 2410, DOI: 10.3390/molecules23102410.
(59) Scheele, T.; Neudecker, T. Investigating the Accuracy of Density Functional Methods for Molecules in Electric Fields. *J. Chem. Phys.* **2023**, *159*, No. 124111, DOI: 10.1063/5.0164372.
(60) Wang, X.; Lu, C.; Yang, M. The Impact of Electron Correlation on Describing Qm/Mm Interactions in the Attendant Molecular Dynamics Simulations of Co in Myoglobin. *Sci. Rep.* **2020**, *10* (1), No. 8539, DOI: 10.1038/s41598-020-65475-2.
(61) Epifanovsky, E.; Gilbert, A. T. B.; Feng, X.; Lee, J.; Mao, Y.; Mardirossian, N.; Pokhilko, P.; White, A. F.; Coons, M. P.; Dempwolff, A. L.; Gan, Z.; Hait, D.; Horn, P. R.; Jacobson, L. D.; Kaliman, I.; Kussmann, J.; Lange, A. W.; Lao, K. U.; Levine, D. S.; Liu, J.; McKenzie, S. C.; Morrison, A. F.; Nanda, K. D.; Plasser, F.; Rehn, D. R.; Vidal, M. L.; You, Z. Q.; Zhu, Y.; Alam, B.; Albrecht, B. J.; Aldossary, A.; Alguire, E.; Andersen, J. H.; Athavale, V.; Barton, D.; Begam, K.; Behn, A.; Bellonzi, N.; Bernard, Y. A.; Berquist, E. J.; Burton, H. G. A.; Carreras, A.; Carter-Fenk, K.; Chakraborty, R.; Chien, A. D.; Closser, K. D.; Cofer-Shabica, V.; Dasgupta, S.; de Wergifosse, M.; Deng, J.; Diedenhofen, M.; Do, H.; Ehlert, S.; Fang, P. T.; Fatehi, S.; Feng, Q.; Friedhoff, T.; Gayvert, J.; Ge, Q.; Gidofalvi, G.; Goldey, M.; Gomes, J.; Gonzalez-Espinoza, C. E.; Gulania, S.; Gunina, A. O.; Hanson-Heine, M. W. D.; Harbach, P. H. P.; Hauser, A.; Herbst, M. F.; Hernandez Vera, M.; Hodecker, M.; Holden, Z. C.; Houck, S.; Huang, X.; Hui, K.; Huynh, B. C.; Ivanov, M.; Jasz, A.; Ji, H.; Jiang, H.; Kaduk, B.; Kahler, S.; Khistyaev, K.; Kim, J.; Kis, G.; Klunzinger, P.; Koczor-Benda, Z.; Koh, J. H.; Kosenkov, D.; Koulias, L.; Kowalczyk, T.; Krauter, C. M.; Kue, K.; Kunitsa, A.; Kus, T.; Ladjanszki, I.; Landau, A.; Lawler, K. V.; Lefrancois, D.; Lehtola, S.; Li, R. R.; Li, Y. P.; Liang, J.; Liebenthal, M.; Lin, H. H.; Lin, Y. S.; Liu, F.; Liu, K. Y.; Loipersberger, M.; Luenser, A.; Manjanath, A.; Manohar, P.; Mansoor, E.; Manzer, S. F.; Mao, S. P.; Marenich, A. V.; Markovich, T.; Mason, S.; Maurer, S. A.; McLaughlin, P. F.; Menger, M.; Mewes, J. M.; Mewes, S. A.; Morgante, P.; Mullinax, J. W.; Oosterbaan, K. J.; Paran, G.; Paul, A. C.; Paul, S. K.; Pavosevic, F.; Pei, Z.; Prager, S.; Proynov, E. I.; Rak, A.; Ramos-Cordoba, E.; Rana, B.; Rask, A. E.; Rettig, A.; Richard, R. M.; Rob, F.; Rossomme, E.; Scheele, T.; Scheurer, M.; Schneider, M.; Sergueev, N.; Sharada, S. M.; Skomorowski, W.; Small, D. W.; Stein, C. J.; Su, Y. C.; Sundstrom, E. J.; Tao, Z.; Thirman, J.; Tornai, G. J.; Tsuchimochi, T.; Tubman, N. M.; Veccham, S. P.; Vydrov, O.; Wenzel, J.; Witte, J.; Yamada, A.; Yao, K.; Yeganeh, S.; Yost, S. R.; Zech, A.; Zhang, I. Y.; Zhang, X.; Zhang, Y.; Zuev, D.; Aspuru-Guzik, A.; Bell, A. T.; Besley, N. A.; Bravaya, K. B.; Brooks, B. R.; Casanova, D.; Chai, J. D.; Coriani, S.; Cramer, C. J.; Cserey, G.; DePrince, A. E., III; DiStasio, R. A., Jr.; Dreuw, A.; Dunietz, B. D.; Furlani, T. R.; Goddard, W. A., III; Hammes-Schiffer, S.; Head-Gordon, T.; Hehre, W. J.; Hsu, C. P.; Jagau, T. C.; Jung, Y.; Klamt, A.; Kong, J.; Lambrecht, D. S.; Liang, W.; Mayhall, N. J.; McCurdy, C. W.; Neaton, J. B.; Ochsenfeld, C.; Parkhill, J. A.; Peverati, R.; Rassolov, V. A.; Shao, Y.; Slipchenko, L. V.; Stauch, T.; Steele, R. P.; Subotnik, J. E.; Thom, A. J. W.; Tkatchenko, A.; Truhlar, D. G.; Van Voorhis, T.; Wesolowski, T. A.; Whaley, K. B.; Woodcock, H. L., III; Zimmerman, P. M.; Faraji, S.; Gill, P. M. W.; Head-Gordon, M.; Herbert, J. M.; Krylov, A. I. Software for the Frontiers of Quantum Chemistry: An Overview of Developments in the Q-Chem 5 Package. *J. Chem. Phys.* **2021**, *155*, No. 084801.
(62) Claudino, D.; Mayhall, N. J. Automatic Partition of Orbital Spaces Based on Singular Value Decomposition in the Context of Embedding Theories. *J. Chem. Theory Comput.* **2019**, *15*, 1053−1064.
(63) Khaliullin, R. Z.; Cobar, E. A.; Lochan, R. C.; Bell, A. T.; Head-Gordon, M. Unravelling the Origin of Intermolecular Interactions Using Absolutely Localized Molecular Orbitals. *J. Phys. Chem. A* **2007**, *111*, 8753−8765.
(64) Stuyver, T.; Huang, J.; Mallick, D.; Danovich, D.; Shaik, S. Titan: A Code for Modeling and Generating Electric Fields-Features and Applications to Enzymatic Reactivity. *J. Comput. Chem.* **2020**, *41*, 74−82.
(65) Clarys, T.; Stuyver, T.; De Proft, F.; Geerlings, P. Extending Conceptual Dft to Include Additional Variables: Oriented External Electric Field. *Phys. Chem. Chem. Phys.* **2021**, *23*, 990−1005.

(66) Matczak, P. A Test of Various Partial Atomic Charge Models for Computations on Diheteroaryl Ketones and Thioketones. *Computation* **2016**, *4*, No. 3, DOI: 10.3390/computation4010003.
(67) Mehta, N.; Martin, J. M. L. On the Sensitivity of Computed Partial Charges toward Basis Set and (Exchange-)Correlation Treatment. *J. Comput. Chem.* **2024**, *45*, 1017−1032.
(68) Vaissier Welborn, V.; Head-Gordon, T. Electrostatics Generated by a Supramolecular Capsule Stabilizes the Transition State for Carbon-Carbon Reductive Elimination from Gold(Iii) Complex. *J. Phys. Chem. Lett.* **2018**, *9*, 3814−3818.
(69) Frushicheva, M. P.; Mukherjee, S.; Warshel, A. Electrostatic Origin of the Catalytic Effect of a Supramolecular Host Catalyst. *J. Phys. Chem. B* **2012**, *116*, 13353−13360.
(70) Kaphan, D. M.; Levin, M. D.; Bergman, R. G.; Raymond, K. N.; Dean Toste, F. A Supramolecular Microenvironment Strategy for Transition Metal Catalysis. *Science* **2015**, *350*, 1235−1238.
(71) Lu, T. A Comprehensive Electron Wavefunction Analysis Toolbox for Chemists, Multiwfn. *J. Chem. Phys.* **2024**, *161*, No. 082503, DOI: 10.1063/5.0216272.
(72) Lu, T.; Chen, F. Multiwfn: A Multifunctional Wavefunction Analyzer. *J. Comput. Chem.* **2012**, *33*, 580−592.
(73) Stone, A. J. *The Theory of Intermolecular Forces*, 2nd ed.; Oxford University Press: New York, NY, United States of America, 2013.
(74) Case, D. A.; Aktulga, H. M.; Belfon, K.; Cerutti, D. S.; Cisneros, G. A.; Cruzeiro, V. W. D.; Forouzesh, N.; Giese, T. J.; Gotz, A. W.; Gohlke, H.; Izadi, S.; Kasavajhala, K.; Kaymak, M. C.; King, E.; Kurtzman, T.; Lee, T. S.; Li, P.; Liu, J.; Luchko, T.; Luo, R.; Manathunga, M.; Machado, M. R.; Nguyen, H. M.; O'Hearn, K. A.; Onufriev, A. V.; Pan, F.; Pantano, S.; Qi, R.; Rahnamoun, A.; Risheh, A.; Schott-Verdugo, S.; Shajan, A.; Swails, J.; Wang, J.; Wei, H.; Wu, X.; Wu, Y.; Zhang, S.; Zhao, S.; Zhu, Q.; Cheatham, T. E., 3rd; Roe, D. R.; Roitberg, A.; Simmerling, C.; York, D. M.; Nagan, M. C.; Merz, K. M., Jr. Ambertools. *J. Chem. Inf. Model.* **2023**, *63*, 6183−6191.
(75) Caleman, C.; van Maaren, P. J.; Hong, M.; Hub, J. S.; Costa, L. T.; van der Spoel, D. Force Field Benchmark of Organic Liquids: Density, Enthalpy of Vaporization, Heat Capacities, Surface Tension, Isothermal Compressibility, Volumetric Expansion Coefficient, and Dielectric Constant. *J. Chem. Theory Comput.* **2012**, *8*, 61−74.
(76) Jorgensen, W. L.; Chandrasekhar, J.; Madura, J. D.; Impey, R. W.; Klein, M. L. Comparison of Simple Potential Functions for Simulating Liquid Water. *J. Chem. Phys.* **1983**, *79*, 926−935.
(77) Götz, A. W.; Williamson, M. J.; Xu, D.; Poole, D.; Le Grand, S.; Walker, R. C. Routine Microsecond Molecular Dynamics Simulations with Amber on Gpus. 1. Generalized Born. *J. Chem. Theory Comput.* **2012**, *8*, 1542−1555.
(78) Salomon-Ferrer, R.; Götz, A. W.; Poole, D.; Le Grand, S.; Walker, R. C. Routine Microsecond Molecular Dynamics Simulations with Amber on Gpus. 2. Explicit Solvent Particle Mesh Ewald. *J. Chem. Theory Comput.* **2013**, *9*, 3878−3888.
(79) Darden, T.; York, D.; Pedersen, L. Particle Mesh Ewald: An N·Log(N) Method for Ewald Sums in Large Systems. *J. Chem. Phys.* **1993**, *98*, 10089−10092.
(80) Roe, D. R.; Cheatham, T. E., III Ptraj and Cpptraj: Software for Processing and Analysis of Molecular Dynamics Trajectory Data. *J. Chem. Theory Comput* **2013**, *9*, 3084−3095.
(81) Manetsch, M. T.; Kastner, D.; Kulik, H. J. pyEF: A Python Framework for QM and QM/MM Atom-Wise Electric Field Analysis. 2025 DOI: 10.5281/zenodo.15529327.
(82) Neese, F. Software Update: The Orca Program System—Version 5.0. *WIREs Comput. Mol. Sci.* **2022**, *12* (5), No. e1606, DOI: 10.1002/wcms.1606.
(83) Ufimtsev, I. S.; Martinez, T. J. Quantum Chemistry on Graphical Processing Units. 3. Analytical Energy Gradients, Geometry Optimization, and First Principles Molecular Dynamics. *J. Chem. Theory Comput.* **2009**, *5*, 2619−2628.
(84) Becke, A. D. Density-Functional Thermochemistry. Iii. The Role of Exact Exchange. *J. Chem. Phys.* **1993**, *98*, 5648−5652.
(85) Lee, C.; Yang, W.; Parr, R. G. Development of the Colle-Salvetti Correlation-Energy Formula into a Functional of the Electron Density. *Phys. Rev. B* **1988**, *37*, 785−789.
(86) Stephens, P. J.; Devlin, F. J.; Chabalowski, C. F.; Frisch, M. J. Ab Initio Calculation of Vibrational Absorption and Circular Dichroism Spectra Using Density Functional Force Fields. *J. Phys. Chem. A* **1994**, *98*, 11623−11627.
(87) Grimme, S.; Antony, J.; Ehrlich, S.; Krieg, H. A Consistent and Accurate Ab Initio Parametrization of Density Functional Dispersion Correction (Dft-D) for the 94 Elements H-Pu. *J. Chem. Phys.* **2010**, *132*, No. 154104.
(88) Becke, A. D.; Johnson, E. R. A Density-Functional Model of the Dispersion Interaction. *J. Chem. Phys.* **2005**, *123*, No. 154101.
(89) Weigend, F.; Ahlrichs, R. Balanced Basis Sets of Split Valence, Triple Zeta Valence and Quadruple Zeta Valence Quality for H to Rn: Design and Assessment of Accuracy. *Phys. Chem. Chem. Phys.* **2005**, *7*, 3297−3305.
(90) Barone, V.; Cossi, M. Quantum Calculation of Molecular Energies and Energy Gradients in Solution by a Conductor Solvent Model. *J. Phys. Chem. A* **1998**, *102*, 1995−2001.
(91) Truong, T. N.; Stefanovich, E. A New Method for Incorporating Solvent Effect into the Classical, Ab Initio Molecular Orbital and Density Functional Theory Frameworks for Arbitrary Shape Cavity. *Chem. Phys. Lett.* **1995**, *240*, 253−260.
(92) Klamt, A.; Schüürmann, G. Cosmo: A New Approach to Dielectric Screening in Solvents with Explicit Expression for the Screening Energy and Its Gradient. *J. Chem. Soc., Perkin Trans. 2.* **1993**, 799−805.
(93) Bondi, A. Van Der Waals Volumes and Radii. *J. Phys. Chem. A* **1964**, *68*, 441−451, DOI: 10.1021/j100785a001.
(94) Stone, A. J. Distributed Multipole Analysis: Stability for Large Basis Sets. *J. Chem. Theory Comput.* **2005**, *1*, 1128−1132.
(95) Stone, A. J.; Alderton, M. Distributed Multipole Analysis Methods and Applications. *Mol. Phys.* **2002**, *100*, 221−233.
(96) Tian, L. U.; Fei-Wu, C. Comparison of Computational Methods for Atomic Charges. *Acta Phys.-Chim. Sin.* **2012**, *28*, 1−18.
(97) Han, B.; Isborn, C. M.; Shi, L. Determining Partial Atomic Charges for Liquid Water: Assessing Electronic Structure and Charge Models. *J. Chem. Theory Comput.* **2021**, *17*, 889−901.
(98) Bultinck, P.; Van Alsenoy, C.; Ayers, P. W.; Carbó-Dorca, R. Critical Analysis and Extension of the Hirshfeld Atoms in Molecules. *J. Chem. Phys.* **2007**, *126*, No. 144111, DOI: 10.1063/1.2715563.
(99) Cho, M.; Sylvetsky, N.; Eshafi, S.; Santra, G.; Efremenko, I.; Martin, J. M. L. The Atomic Partial Charges Arboretum: Trying to See the Forest for the Trees. *ChemPhysChem* **2020**, *21*, 688−696.
(100) Liu, F.; Kulik, H. J. Impact of Approximate Dft Density Delocalization Error on Potential Energy Surfaces in Transition Metal Chemistry. *J. Chem. Theory Comput* **2020**, *16*, 264−277.
(101) Chen, L. D.; Bajdich, M.; Martirez, J. M. P.; Krauter, C. M.; Gauthier, J. A.; Carter, E. A.; Luntz, A. C.; Chan, K.; Norskov, J. K. Understanding the Apparent Fractional Charge of Protons in the Aqueous Electrochemical Double Layer. *Nat. Commun.* **2018**, *9*, No. 3202.
(102) Fried, S. D. E.; Zheng, C.; Mao, Y.; Markland, T. E.; Boxer, S. G. Solvent Organization and Electrostatics Tuned by Solute Electronic Structure: Amide Versus Non-Amide Carbonyls. *J. Phys. Chem. B* **2022**, *126*, 5876−5886.
(103) Fried, S. D. E.; Zheng, C.; Mao, Y.; Markland, T. E.; Boxer, S. G. Solvent Organization and Electrostatics Tuned by Solute Electronic Structure: Amide Versus Non-amide Carbonyls. *J. Phys. Chem. B* **2022**, *126*, 5876−5886.
(104) Ponder, J. W.; Wu, C.; Ren, P.; Pande, V. S.; Chodera, J. D.; Schnieders, M. J.; Haque, I.; Mobley, D.; Lambrecht, D. S.; DiStasio, R. A., Jr.; Head-Gordon, M.; Clark, G. N. I.; Margaret, E. J.; Head-Gordon, T. Current Status of the Amoeba Polarizable Force Field. *J. Phys. Chem. B* **2010**, *114*, 2549−2564.
(105) Reinhardt, C. R.; Manetsch, M. T.; Li, W. L.; Roman-Leshkov, Y.; Head-Gordon, T.; Kulik, H. J. Computational Screening of

Putative Catalyst Transition Metal Complexes as Guests in a Ga(4)L(6)(12-) Nanocage. *Inorg. Chem.* **2024**, *63*, 14609−14622.
(106) Weigend, F.; Ahlrichs, R. Balanced basis Sets of Split Valence, Triple Zeta Valence and Quadruple Zeta Valence Quality for H to Rn: Design and Assessment of Accuracy. *Phys. Chem. Chem. Phys.* **2005**, *7*, 3297−3305.

https://doi.org/10.1021/acs.jctc.6c00065
J. Chem. Theory Comput. XXXX, XXX, XXX−XXX